Band gap engineering in pyridyl-functionalized two-dimensional (2D) CuSCN coordination polymers

Jetnipat Songkerdthong,[a] Thanasee Thanasarnsurapong,[b] Adisak Boonchun,[b] David J. Harding,[c] and Pichaya Pattanasattayavong*,[a]

[a] Department of Materials Science and Engineering, School of Molecular Science and Engineering, Vidyasirimedhi Institute of Science and Technology (VISTEC), Rayong 21210, Thailand

[b] Department of Physics, Faculty of Science, Kasetsart University, Bangkok 10900, Thailand

[c] School of Chemistry, Institute of Science, Suranaree University of Technology, Nakhon Ratchasima 30000, Thailand

* Corresponding author: pichaya.p@vistec.ac.th

KEYWORDS: Copper(I) thiocyanate, coordination polymers, 2D materials, ligand modification

ABSTRACT

Copper(I) thiocyanate (CuSCN) has emerged as an excellent hole-transporting semiconductor with applications spanning across electronic and optoelectronic fields. The coordination chemistry of CuSCN allows for extensive structural versatility via ligand modification. In this work, we have developed a synthetic method that reliably produces phase pure $[Cu(SCN)(3\text{-}XPy)]_n$ complexes (Py = pyridyl; X = OMe, H, Br, and Cl) in a 1:1:1 ratio to yield two-dimensional (2D) structures with a Cu-SCN network. The single crystal structure of $[Cu(SCN)(3\text{-}OMePy)]_n$ is also reported herein. Complexes with X = OMe and H show similar structures, in which the 2D layers are analogous to the buckled 2D sheets of silicene or blue phosphorene. On the other hand, for complexes with X = Br and Cl, their rippled 2D structures resemble the puckered 2D sheets found in black phosphorene. The variation of the electron-withdrawing ability of the substituent group is found to systematically shift the electronic energy

levels and band gaps of the complexes, allowing the 2D CuSCN-based materials to display optical absorptions and emissions in the visible range. In addition, first-principles calculations reveal that the drastic change in the electronic levels is a result of the emergence of the Py ligand electronic states below the SCN states. This work demonstrates that the structural, electronic, and optical properties of 2D Cu-SCN networks can be systematically tailored through ligand modification.

DESIGN, SYSTEM, APPLICATION

CuSCN has an extended three-dimensional (3D) network consisting of Cu(I) centers tetrahedrally bridged by bidentate SCN ligands. Structural modification using co-ligands can reduce the dimensionality and shift the electronic and optical properties over a wide range. The 2D structures are of particular interest as they can retain the unique hole-transporting states based on the Cu-S network while introducing novel properties from the co-ligand electronic states. In effect, 3D CuSCN which has a large band gap can be transformed into 2D structures with optical absorptions and emissions in the visible spectrum via ligand engineering. The electronic levels and optical properties of the complexes can be further fine-tuned by controlling the electronic properties of the co-ligands. Such modifications can expand the applications of CuSCN-based materials in optoelectronic devices beyond the current usage of CuSCN as a transparent, non-emissive layer.

1. INTRODUCTION

Copper(I) thiocyanate (CuSCN) is known as a p-type semiconductor; its unique electronic and optical properties in conjunction with solution-processability have made it attractive for an expansive range of applications such as thin-film transistors (TFTs),[1–4] organic light-emitting diodes (OLEDs),[5–8] organic photovoltaics (OPVs)[9–11] and perovskite solar cells (PSCs).[12–15] The key characteristics of CuSCN are excellent hole transport properties and a wide band gap (>3.5 eV) yielding high optical transparency. Recently, the importance of coordination chemistry in CuSCN has been realized, leading to a deeper understanding of its structure-property relationships and novel strategies to improve the performance of CuSCN-based devices, such as by antisolvent treatment or SCN^- defect passivation.[16–18] CuSCN is in fact a 3D coordination polymer (CP) consisting of Cu(I), a soft acceptor, tetrahedrally linked by the bidentate SCN^-, which is a soft donor.[19] Its structure thus allows for a diverse range of structural modifications via ligand (L) engineering. Cu(SCN)-co-L complexes with tunable 2D, 1D and 0D structures can be obtained by controlling four key factors including: (i) geometry of the metal center, (ii) Cu:SCN:L ratio, (iii) steric effects, and (iv) supramolecular interactions.[20]

Among the possible dimensionalities of Cu(SCN)-co-L complexes, the 2D sheet structure is of particular interest because it retains the extended Cu-S network which is the main pathway for the hole transport; in contrast, the lower dimensionalities (1D and 0D) reduce such network to localized states, greatly restricting the carrier transport properties.[20] In the 2D structures, Cu and SCN typically form the main 2D sheets while the co-ligands can coordinate to: (i) both the top and bottom sides of the sheet, resulting in rippled structures;[21] or (ii) only one side, resulting in relatively flat sheets.[22] The differences depend on the size and the steric repulsion of the ligands. In addition, adjusting the organic ligands is a powerful tool to tailor the properties further because it affects not only the structural and chemical properties but also optical and electronic properties.[22,23] For example, Miller *et al*. reported the synthesis of complexes comprising CuSCN and N-donor ligands and found that aromatic ligands allow CuSCN complexes to show absorption or emission properties in the visible region while

aliphatic ligands retain the optical transparency of the parent CuSCN.[21] The ligand addition into the 2D CuSCN network also affects the band gap and introduces additional features such as extra light absorption, better dispersion/dissolution in solvent, favorable affinity for target chemicals for sensing, and defects healing in multi-layer electronic devices.[24,25] Moreover, complexes of CuSCN and ligands have been explored as intermediates to obtain CuSCN with enhanced crystallinity.[26]

Pyridine (Py) is a simple ligand with an N donor that can coordinate with CuSCN. Krautscheid *et al.* reported the structure of $[Cu(SCN)(Py)]_n$ in 1998.[27] After that, a variety of structures were reported using different Py derivatives and controlling the Cu:SCN:Py ratio.[21] The 1:1:1 ratio is required to obtain the 2D structure; however, achieving this ratio through synthesis is not trivial. The solubility of CuSCN is limited, and it typically requires unconventional solvents (S- or N-containing compounds) to dissolve and process into high-quality films for devices whereas more aggressive solvents can induce defects such as structural mismatch from polymorphism and Cu(II) impurities from unintentional oxidation.[28] Solvents used for CuSCN include diethyl sulfide (DES) and dipropyl sulfide (DPS), but these can also affect the structure of CuSCN because they can act as ligands and coordinate Cu(I), becoming trapped inside or causing defects.[17,18,29] As a result, the synthesis of Cu(SCN)-co-L complexes, when the ligands are liquids at room temperature, as in the case of Py and some derivatives, usually proceeds by reacting solid CuSCN with the neat ligands (i.e., a large excess of ligands), commonly producing complexes with a 1:1:2 ratio of Cu:SCN:Py, resulting in the lower 1D dimensionality. In this work, CuSCN complexes with different Py derivatives were reliably obtained in the required 1:1:1 ratio using our synthetic procedure. A series of substituents with different electron-donating/withdrawing ability at the 3-position of Py (3-XPy, where X = OMe, H, Br, or Cl) were also investigated for their effects on the structural, electronic, optical, and electrical properties. The single-crystal structure of $[Cu(SCN)(3\text{-}OMePy)]_n$ was also obtained. The electronic energy levels of 2D CuSCN could be systematically tuned by varying the ligands.

2. RESULTS AND DISCUSSION

2.1. Synthesis and structural characterization of $[Cu(SCN)(3\text{-}XPy)]_n$

To elucidate the interplay between structure and properties in Cu(SCN)-co-L complexes, we synthesized a series of $[Cu(SCN)(3\text{-}XPy)]_n$ coordination polymers where X = OMe, H, Br, or Cl (listed in order of decreasing electron-donating ability of 3-XPy). This systematic variation allowed us to probe the impact of the electron-accepting/donating ability on both the structural and opto/electronic properties of CuSCN-based CPs. The full methods are described in the experimental section.

$[Cu(SCN)(3\text{-}XPy)]_n$ compounds are the products of reactions between CuSCN and 3-XPy, which can yield different structures, influenced by the Cu:SCN:3-XPy ratio, and often result in mixed products. Optimizing the synthetic conditions is therefore crucial for reliably achieving a 1:1:1 ratio in order to realize the controlled production of our target 2D CPs based on $[Cu(SCN)(3\text{-}XPy)]_n$. As mentioned above, working with CuSCN has limitations due to the insolubility of CuSCN in many solvents. Since 3-XPy ligands studied in this work are liquid at room temperature and can in fact dissolve CuSCN, the usual synthetic route is to add CuSCN to neat 3-XPy. For the initial study, we performed such a reaction between CuSCN and neat 3-ClPy at room temperature and 70 °C to investigate the impact of temperature on the synthesis of $[Cu(SCN)(3\text{-}ClPy)_m]_n$. We found that attenuated total reflectance infrared spectroscopy (ATR-IR) can provide a quick and simple way to distinguish the products as $[Cu(SCN)(3\text{-}ClPy)]_n$ (1:1:1 ratio) and $[Cu(SCN)(3\text{-}ClPy)_2]_n$ (1:1:2 ratio) show distinct peaks for the ν(CN) vibration at 2120 cm^{-1} and 2096 cm^{-1}, respectively [**Figure S1**, Electronic Supplementary Information (ESI)]. The ATR-IR spectra of the products at both temperatures reveal a peak at 2096 cm^{-1}, indicating that the reaction between CuSCN and neat 3-ClPy favors the formation of $[Cu(SCN)(3\text{-}ClPy)_2]_n$ which has a 1D structure.[30]

To obtain the desired 1:1:1 ratio, we found that carrying out the reactions in acetonitrile (MeCN) reliably gave the target products. Partially dissolved CuSCN in MeCN gradually

transformed into $[Cu(SCN)(3\text{-ClPy})]_n$ when reacting with an excess of 3-ClPy. The ATR-IR spectrum exhibited the ν(CN) at 2120 cm^{-1}, suggesting the formation of the targeted 1:1:1 2D CP. We note that if 1 equivalent of the ligand was added, the reaction instead yielded a mixture of the 1:1:1 complex and unreacted CuSCN with the latter showing a distinctive ν(CN) peak at 2172 cm^{-1}, characteristic of β-CuSCN.[31] Employing MeCN as the solvent gave a series of $[Cu(SCN)(3\text{-XPy})]_n$ complexes, where X = OMe, H, Br, or Cl. From the ATR-IR spectra as shown in **Figure 1**, the ν(CN) vibrational peak was consistently observed at 2117 cm^{-1}, except for $[Cu(SCN)(3\text{-ClPy})]_n$, where a slight shift was noted at 2120 cm^{-1}. Furthermore, in **Figure S2** (ESI), the phases of the complexes were verified by matching the measured powder X-ray diffraction (PXRD) pattern with reference data simulated from the reported single crystal X-ray diffraction (SC-XRD) data of $[Cu(SCN)(3\text{-ClPy})]_n$,[21] $[Cu(SCN)(3\text{-BrPy})]_n$,[21] and $[Cu(SCN)(Py)]_n$.[27] As for $[Cu(SCN)(3\text{-OMePy})]_n$, the SCXRD data was collected in this work as described below.

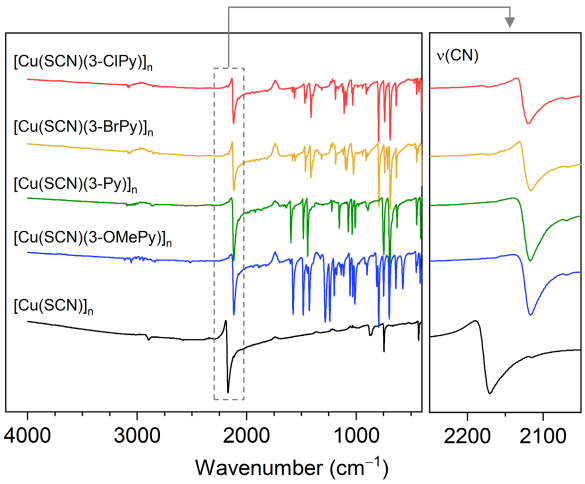

Figure 1. ATR-IR spectra $[Cu(SCN)(3\text{-XPy})]_n$ complexes. The ν(CN) region used for identifying complexes with the 1:1:1 ratio is shown in the right panel. Data of $[Cu(SCN)]_n$ which was also processed with MeCN (without any additional ligands) is shown as a reference.

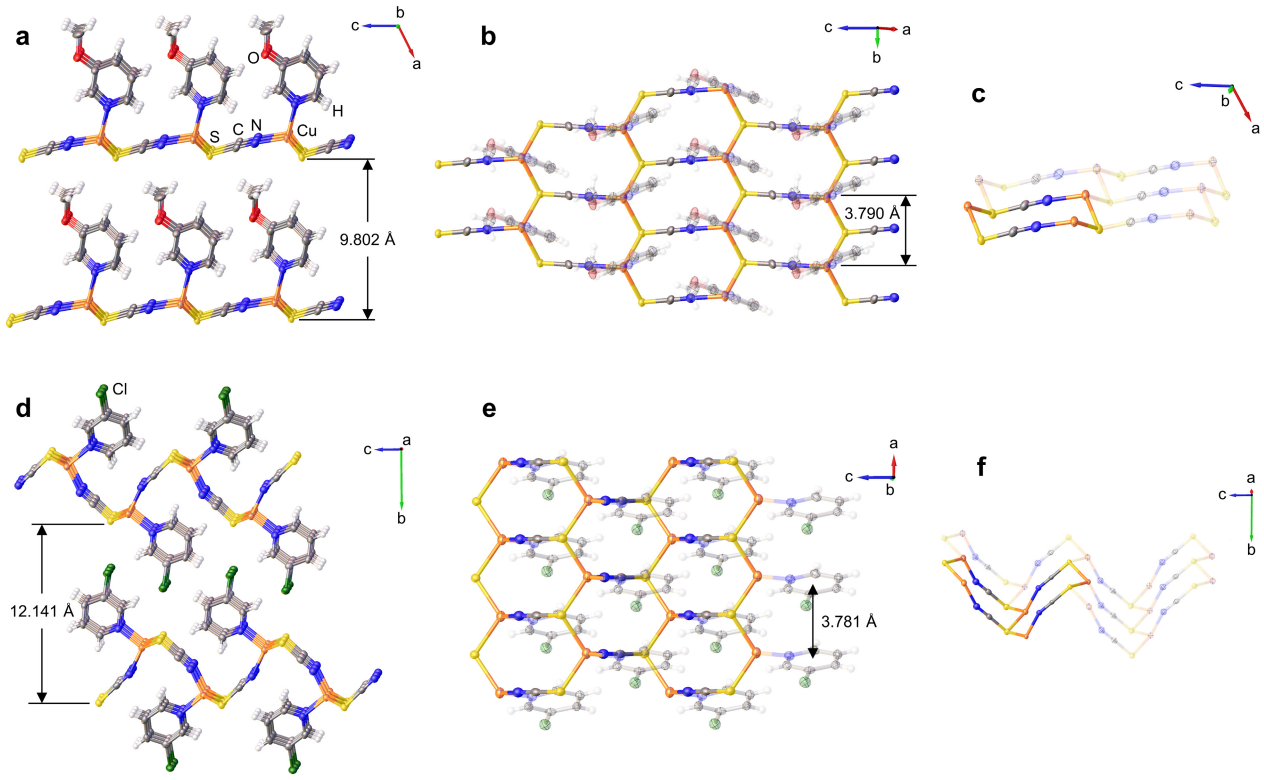

Figure 2. 2D structure of $[Cu(SCN)(3\text{-}OMePy)]_n$ shown as (a) edge-on, (b) face-on, and (c) only the Cu-SCN network with the 3-OMePy ligands omitted, showing the 2D buckled sheet. For comparison, the 2D structure of $[Cu(SCN)(3\text{-}ClPy)]_n$ shown as (d) edge-on, (e) face-on, and (f) only the Cu-SCN network with the 3-ClPy ligands omitted, showing the 2D puckered/rippled sheet. Interlayer distances are noted in (a) and (d); π-π distances are shown in (b) and (e).

The crystal structure of $[Cu(SCN)(3\text{-}OMePy)]_n$ was determined through SCXRD. The crystallographic data and refinement parameters are reported in **Table S1** (ESI) (CCDC no. 2329055). The structure reveals a 2D sheet formed by the linkage of the Cu-SCN network as shown in **Figure 2a-b**. This 2D structure is similar to $[Cu(SCN)(Py)]_n$ (**Figure S3**, ESI) with a relatively flat topology of the 2D Cu-SCN honeycomb network, in which the co-ligands coordinate to only one side of the sheet. Interestingly, the Cu-SCN network (**Figure 2c**) resembles that of 2D silicene/germanene[32] or the 2D buckled structure of blue

phosphorene/gray arsenene,[33,34] but elongated in one direction due to linear nature of SCN. In contrast, the other two compounds, $[Cu(SCN)(3\text{-}BrPy)]_n$ and $[Cu(SCN)(3\text{-}ClPy)]_n$, display a 2D structure with notable undulation as the ligands coordinate to both sides of the Cu-SCN layer (**Figure 2d-e** and **Figure S3**, ESI). In this case, the 2D Cu-SCN network (**Figure 2f**) resembles that of the 2D puckered structure of black phosphorene or puckered arsenene.[33,34]

Table 1. List of selected bond length (Å), distance (Å), bond angle (deg), and geometry index for four-coordinate parameters (τ_4)[35] of $[Cu(SCN)(3\text{-}XPy)]_n$.

Complexes	**$[Cu(SCN)(3\text{-}OMePy)]_n$**	**$[Cu(SCN)(Py)]_n$**	**$[Cu(SCN)(3\text{-}BrPy)]_n$**	**$[Cu(SCN)(3\text{-}ClPy)]_n$**
Distance (Å)				
Cu1-S1	2.3497(13)	2.358(2)	2.3585(9)	2.3310(7)
Cu1-N1	1.937(4)	1.957(5)	1.974(3)	1.974(2)
Cu1-N2	2.045(3)	2.054(5)	2.065(3)	2.064(2)
Cu1-S1*	2.3755(13)	2.377(2)	2.3376(10)	2.3553(6)
Py···Py	3.7899(3)	3.855(2)	3.8166(3)	3.7814(1)
Interlayer	9.8023(8)	8.312(4)	12.1440(8)	12.1415(4)
Angle (deg)				
S1-Cu1-N1	111.33(12)	110.14(15)	117.51(9)	116.82(7)
S1-Cu1-N2	111.56(11)	111.42(12)	102.05(8)	108.88(6)
S1-Cu1-S1*	106.66(4)	109.00(6)	108.73(4)	107.59(3)
N1-Cu1-N2	112.52(15)	111.1(2)	102.10(12)	102.92(8)
N1-Cu1-S1*	106.18(13)	105.9(14)	116.21(9)	117.18(7)
N2-Cu1-S1*	108.22(11)	109.08(12)	108.68(8)	102.02(6)
Index				
τ_4	0.964	0.975	0.896	0.894

Note: N2 is the nitrogen atom of the pyridine derivatives; * denotes a symmetry generated element (S1* is the sulfur atom of the adjacent asymmetric unit).

All structures discussed herein belong to the monoclinic crystal system. The selected bond lengths and angles surrounding the Cu center are listed in **Table 1** for comparison. When compared to 3R-β-CuSCN with Cu-N(CS) and Cu-S(CN) bond lengths of 1.92 and 2.34 Å, respectively, the distances between Cu and SCN ligands in the complexes are slightly larger.

The bond length between Cu and 3-XPy changed slightly with the electron-donating strength of the co-ligands. 3-OMePy, with the highest electron-donating ability, showed the shortest Cu-L bond length at 2.04 Å while that of Py was 2.05 Å. 3-BrPy and 3-ClPy with stronger electron-withdrawing effects of the halogens displayed longer bonds at 2.06-2.07 Å. This indicates that the stronger electron-withdrawing substitutional groups reduce the electron density on the N-atom of Py, thus weakening the bond.

The geometry index for a four-coordinate complex (τ_4) can be calculated using **Eq 1**:

$$\tau_4 = \frac{360° - (A_\alpha + A_\beta)}{141°} \quad (1)$$

where A_α and A_β are the two largest angles around the four-coordinate species [Cu(I) in this case].[35] The values of τ_4 ranges between 1 and 0 for perfect tetrahedral and square planar geometries, respectively. Intermediate structures, including trigonal pyramidal and seesaw geometries, fall within these two values. In the buckled 2D structures of $[Cu(SCN)(3\text{-}OMePy)]_n$ and $[Cu(SCN)(Py)]_n$, τ_4 was high at 0.96 and 0.98, respectively. These values are essentially identical to that of β-CuSCN at 0.98. The substitution with Cl and Br led to the top-bottom alternating arrangement, resulting in a large undulation of the Cu-SCN network in $[Cu(SCN)(3\text{-}ClPy)]_n$ and $[Cu(SCN)(3\text{-}BrPy)]_n$ with τ_4 of 0.89 and 0.90, respectively. This shows a larger structural distortion around Cu(I) when compared to the parent β-CuSCN.

Supramolecular interactions arising from the co-ligands play a crucial role in modulating the structure of $[Cu(SCN)(3\text{-}XPy)]_n$ complexes. The aromatic rings of the co-ligands facilitate π-π interactions, with centroid-to-centroid distances of 3.79, 3.86, 3.82, and 3.78 Å for X = OMe, H, Br, and Cl, respectively, as shown in **Table 1**. Notably, these distances are considerably smaller than 4.00 Å,[36] indicating significant π-π interactions that help stabilize the 2D sheet of the Cu-SCN network as shown in our earlier analysis.[20] Furthermore, intermolecular interactions between the layers were noted in 2D $[Cu(SCN)(3\text{-}OMePy)]_n$; these interactions involve a hydrogen from the methoxy group and the C atom of the SCN ligand in the adjacent 2D layer, resulting in a C-H···C distance of 2.78 Å (**Figure S3a**, ESI), which is

smaller than the combined van der Waals (vdW) radii of C and H at 2.90 Å. Intramolecular interactions between C-H···C of the aromatic ligand and C in the SCN unit within the same 2D layer were also observed at a distance of 2.71 Å for $[Cu(SCN)(3\text{-}OMePy)]_n$ and $[Cu(SCN)(Py)]_n$ (**Figure S3a-b**, ESI). Additionally, there are strong C-H···O interactions involving the methoxy group and a pyridyl C-H of $[Cu(SCN)(3\text{-}OMePy)]_n$ with a distance of 2.49 Å (vdW radii of O and H are 2.72 Å).

As for the undulating, puckered (or rippled) 2D sheets, intramolecular C-H···C interactions were also observed within the layers, involving the C-H bond of the aromatic ring and the C atom of the SCN ligand within the same layer. Distances of 2.80 and 2.81 Å were noted for $[Cu(SCN)(3\text{-}BrPy)]_n$ and 2.85 and 2.81 Å for $[Cu(SCN)(3\text{-}ClPy)]_n$. As the halogen-substituted co-ligands coordinate from both sides of the 2D Cu-SCN network, these intramolecular interactions appear to lock the pyridine rings into the grooves of the undulating sheets, as depicted in **Figure S3c-d.**

2.2. Thermal stability of $[Cu(SCN)(3\text{-}XPy)]_n$

$[Cu(SCN)(3\text{-}XPy)]_n$ complexes were subjected to thermogravimetric analysis (TGA) to study their thermal stability as shown in **Figure 3a** and **Figure S4a-d** (ESI). The TGA results of all four complexes showed a two-step decomposition process. The first mass loss, occurring within the temperature range of 80 to 160 °C, was attributed to the transformation of $[Cu(SCN)(3\text{-}XPy)]_n$ into $[Cu(SCN)]_n$, (that is, the loss of the 3-XPy ligands) as validated by ATR-IR. Accordingly, the second mass loss, occurring between 400 to 430 °C, could be ascribed to the decomposition of CuSCN. The data of CuSCN processed with MeCN (without any ligands) shown as a reference in **Figure S4e** (ESI) confirmed the assignment of the second decomposition event. The percentages of the initial mass loss during the first decomposition were determined from TGA profiles as 47.4%, 39.0%, 55.9%, and 47.6% for complexes with X = OMe, H, Br, and Cl, respectively. When the molar ratios were calculated,

all complexes were found to have the required 1:1:1 ratio of Cu:SCN:3-XPy, further corroborating that our method can reliably yield the products with the desired stoichiometry.

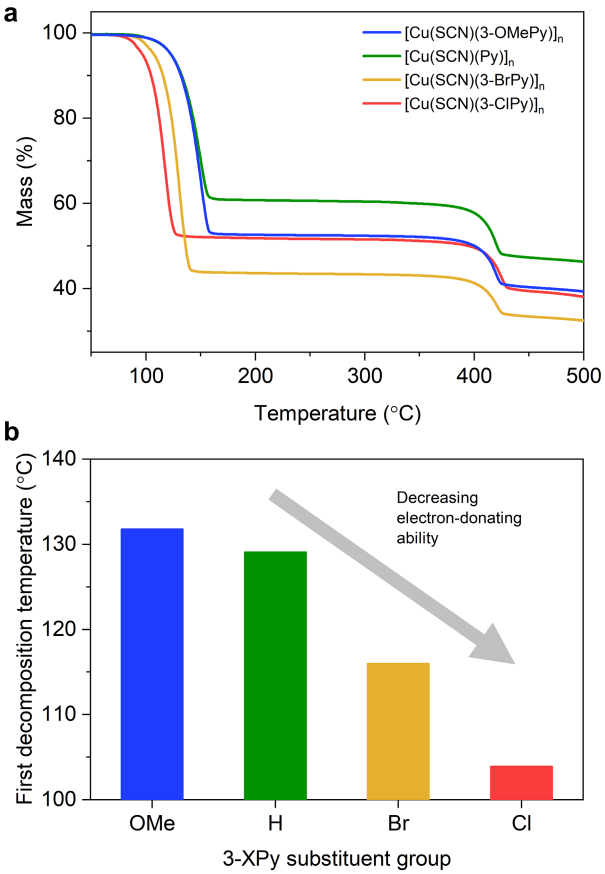

Figure 3. (a) TGA results of $[Cu(SCN)(3\text{-}XPy)]_n$ complexes. (b) Comparison of the first decomposition temperature amongst the complexes.

The Cl-substituted Py, which has the weakest electron-donating ability, results in the lowest thermal stability as $[Cu(SCN)(3\text{-}ClPy)]_n$ started to decompose at 104 °C. For the three other complexes, the decomposition started at higher temperatures at 116, 129, and 132 °C for Br-, H-, and OMe-substituted Py ligands, respectively. $[Cu(SCN)(3\text{-}OMePy)]_n$, with the strongest electron-donating ability, exhibited the highest thermal stability. When the onset temperatures of the first decomposition are plotted in **Figure 3b**, it is apparent how the thermal

stability of the complexes changes with the electron-donating ability. Following the discussion in the previous section, the higher electron-withdrawing strength of the substituent leads to lower electron density on the pyridine ring, thus weakening the Cu-N bond and permitting decomposition at a lower temperature.

2.3. Electronic and optical properties of $[Cu(SCN)(3\text{-}XPy)]_n$

To elucidate the impact of varying the substituent group of the pyridine derivatives on the electronic energy levels, we characterized the complexes (as powders) with ultraviolet-visible spectroscopy (UV-Vis), photoluminescence spectroscopy (PL), and photoelectron yield spectroscopy (PYS). The UV-Vis reflectance spectra, shown in **Figure 4a**, exhibited a systematic red shift from the UV range into the blue with the decreasing electron-donating ability of Py (that is, with the increasing electron-withdrawing strength of the substituent). For example, the 50% reflectance edge was shifted from 337 nm for CuSCN to 400, 405, 433, and 440 nm for complexes with X = OMe, H, Br, and Cl, respectively. From the UV-Vis data, the optical band gaps (E_g^{opt}) can be determined utilizing the Tauc plot as shown in **Figure 4b**. $[Cu(SCN)]_n$ displays a large E_g^{opt} of 3.65 eV, a well-known characteristic. In accordance with the red shift in the UV-Vis spectra, E_g^{opt} of the complexes became successively smaller: 3.05, 3.03, 2.84, and 2.79 eV, respectively for the same order of substituent group as mentioned above. This represents a band gap tuning range between 0.65 and 0.86 eV. The significant decrease in E_g^{opt} is due to the emergence of additional electronic states due to the ligands, which lie below the π^* states of SCN (further discussed in the computational section below). These ligand electronic states then serve as electron acceptor states for the metal-to-ligand charge transfer (MLCT) transitions upon light absorption, effectively lowering the conduction band edge of $[Cu(SCN)(3\text{-}XPy)]_n$ complexes.

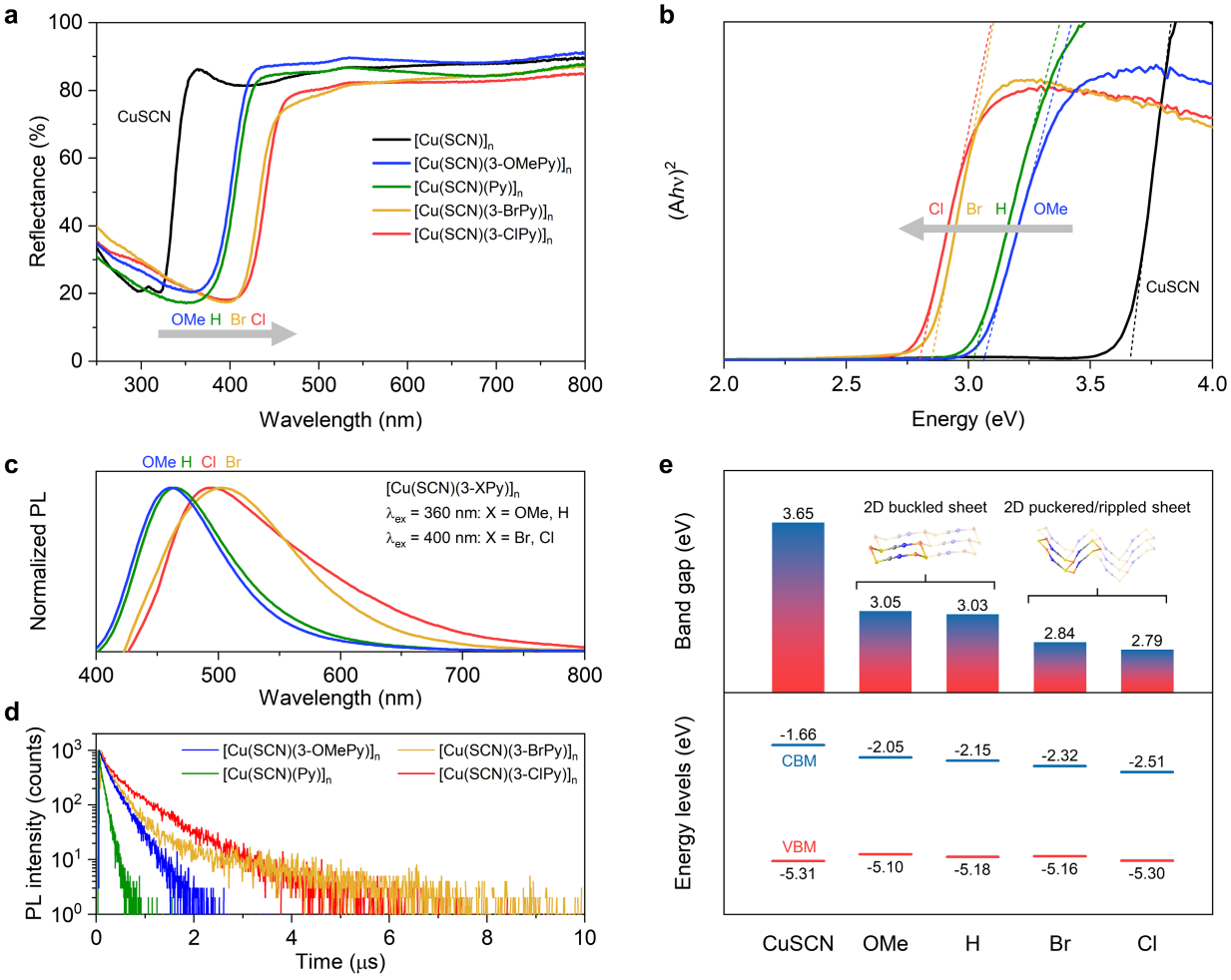

Figure 4. (a) UV-Vis reflectance spectra, (b) Tauc plot for the determination of the optical band gaps, (c) PL spectra, and (d) time-resolved PL data of $[Cu(SCN)(3\text{-}XPy)]_n$ and $[Cu(SCN)]_n$ powder samples. (e) Summary of the optical band gaps and electronic energy levels (valence band maximum or VBM and conduction band minimum or CBM).

Photoluminescence (PL) spectra were also acquired from powder samples of the complexes, with excitation wavelengths (λ_{ex}) adjusted to correspond with the absorption peaks in the UV-Vis spectra, specifically λ_{ex} = 360 nm for $[Cu(SCN)(3\text{-}OMePy)]_n$ and $[Cu(SCN)(Py)]_n$ and 400 nm for $[Cu(SCN)(3\text{-}BrPy)]_n$ and $[Cu(SCN)(3\text{-}ClPy)]_n$. We note that, for CuSCN, Miller *et al*. previously reported a weak emission centered at 400 nm (λ_{ex} = 241 nm);[21] however, in our experiments, the PL intensity was too weak to be observed. For 3-XPy-modified

complexes, the PL peaks were found at 462, 466, 504, and 494 nm for X = OMe, H, Br, and Cl, respectively (**Figure 4c**). The emissions were of the phosphorescent type with PL lifetimes of 258, 88, 337, and 433 ns, respectively, as measured by time-resolved PL (**Figure 4d**). Clearly, modifying CuSCN with these Py ligands enabled the complexes to be active in the visible region both for absorption and emission properties. The PL could be attributed to the ligand-to-metal charge transfer (LMCT) transitions involving the π^* orbitals of the aromatic ligands and the Cu(I) metal center (i.e., the reverse of the absorption). The PL red shift signifies that the stronger the electron-withdrawing ability of the substituent group the lower the π^* energy level of the 3-XPy ligands. We remark that this is the first report of PL emissions from 2D structures based on Py-modified Cu-SCN networks. In the previous study of emissions from 3-BrPy- and 3-ClPy-modified CuSCN complexes, only data of those with a 1:1:2 ratio (structures not specified, but likely 1D type) were reported with emission peaks at 529 and 524 nm, respectively.[21] Also, in that report as well as in our current work, 3-BrPy led to an emission at a longer wavelength compared to 3-ClPy (despite the latter exhibiting a smaller band gap). This suggests that the excited states of the 3-BrPy-modified complexes may undergo a higher degree of molecular reorganization. Overall, the PL emissions of the 2D CuSCN structures reported here fall in the intermediate range between the emissions of the parent 3D CuSCN and the formerly described 1D structures.

To construct the energy band diagrams of the complexes, their valence band maximum (VBM) energy levels were measured with photoelectron yield spectroscopy (PYS). We also varied the intensity of the excitation source to obtain reliable VBM levels as shown in **Figure S5** (ESI). Then, the conduction band minimum (CBM) energy levels could be estimated by: CBM = VBM + E_g^{opt}, with the resulting schematic energy diagrams displayed in **Figure 4e**. A discernible pattern emerges: an increase in the electron-accepting strength of the substituent (which reduces the electron-donating ability of Py) leads to a downward shift in the energy levels. This is especially true for the CBM levels which are directly related to the electronic states of the co-ligands.

2.4. First-principles study of electronic band structures and density of states

To validate our discussions based on the experimental data, we studied the 2D CuSCN complexes from first-principles using density functional theory (DFT). The DFT calculations with a plane-wave basis set were performed with both the PBE functional and HSE06 hybrid functional while considering the vdW interactions with DFT-D3 correction. By comparing the lattice parameters and the band gap values (**Table S2**, ESI), it is evident that the HSE06 hybrid functional yielded better results that were closer to the experimental data, especially for the band gap values; the PBE functional resulted in highly underestimated band gap values, which is a well-known problem with this functional.[37] Therefore, the discussions herein are based on results using HSE06 hybrid functional.

The computed electronic band structures are plotted in **Figure S6** (ESI). Comparison against 3R-β-CuSCN with a VB width of 2.5 eV, the 2D complexes showed smaller VB widths of 1.7-1.8 eV. This can be ascribed to the reduction in the dimensionality of the structure. The 3D CuSCN structure is constructed from covalent/coordination bonds that allow extended interactions whereas the 2D structures are held together via weaker intermolecular interactions between the layers, restricting the delocalization between the 2D Cu-SCN sheets. However, the 2D structures still exhibited large dispersions in the VB states; if the dimensionality is further reduced to 1D or 0D, the VB becomes flat, indicating localized states as shown in our earlier study.[20] Another key feature of the $[Cu(SCN)(3\text{-}XPy)]_n$ complexes is that their CBM states are formed by the Py ligands (gray lines in **Figure S6**) instead of the SCN states (blue lines in **Figure S6**) as in the case of CuSCN. This explains the significant decrease in the band gap size upon coordination of the Py ligands: there exist additional electronic states from the ligands which lie at much lower energies than the SCN states. We also observe that the band gap decreases in the order of X = OMe, H, Br, and Cl, which is the same trend found in the experiment described in the previous section.

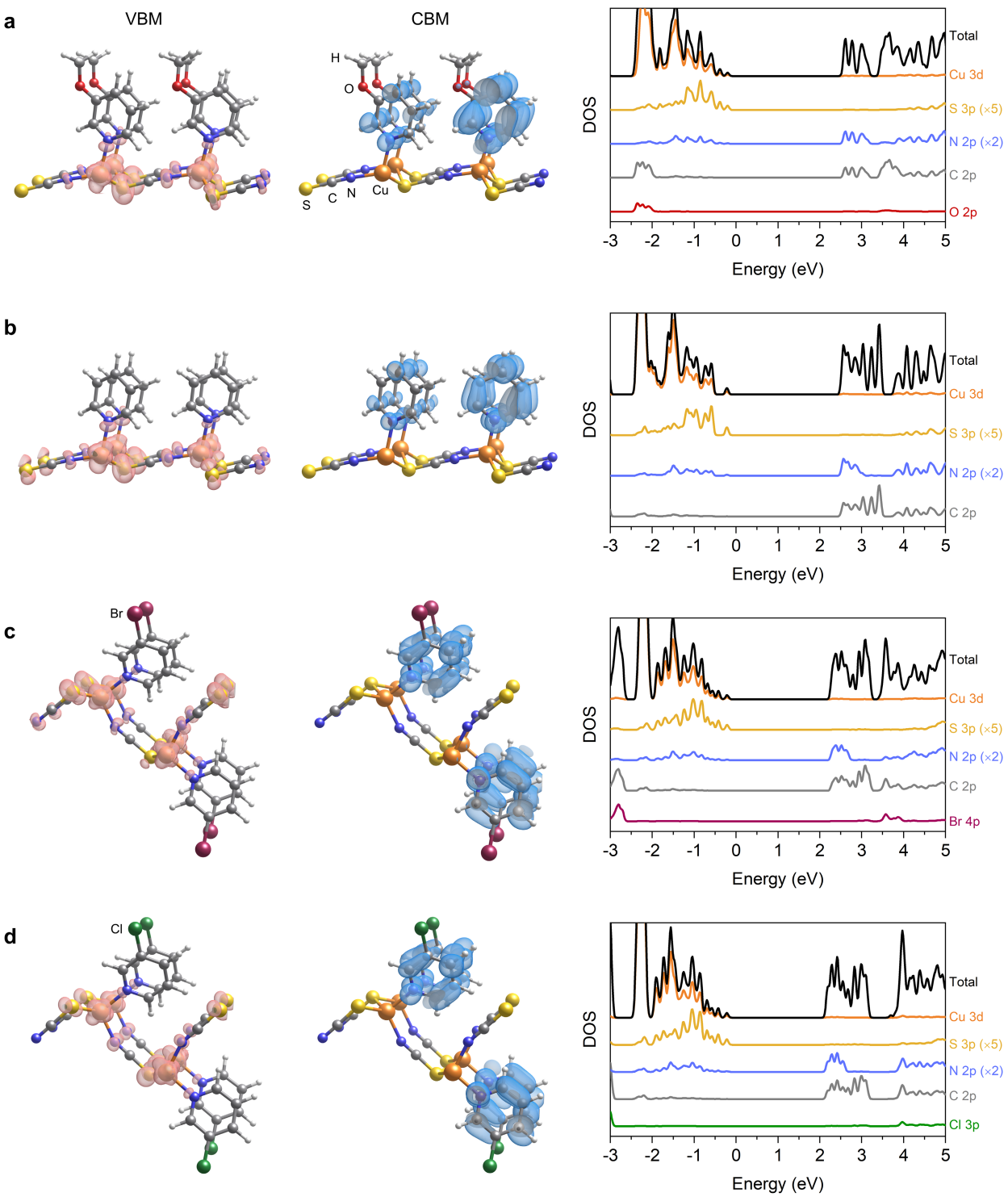

Figure 5. Isosurfaces of VBM and CBM states and plots of density of states (DOS) for 2D $[Cu(SCN)(3\text{-}XPy)]_n$ complexes with X = (a) OMe, (b) H, (c) Br, and (d) Cl, respectively

To visualize the VBM and CBM states, their isosurface charge densities are displayed in **Figure 5** alongside the density of states (DOS) plots. A similar set of reference data for 3R-β-CuSCN is included in **Figure S7** (ESI), showing clearly that the VBM is formed mainly by the Cu-S network whereas the CBM involves the SCN π* state. For the 2D complexes, the VBM states retain the Cu-S character, but the CBM states change drastically involving π* orbitals of the aromatic Py rings. This also suggests a strong charge transfer character. From the DOS plots, the substituent atoms are not involved directly in the VBM or CBM states but appear deep in the VBs or high in the CBs. Therefore, their influence on the electronic properties is through increasing or decreasing the electron density on the Py rings, which in turn affects the coordination between Py and Cu(I).

.

3. CONCLUSIONS

In summary, we successfully synthesized 2D coordination polymers, $[Cu(SCN)(3\text{-}XPy)]_n$ (where X = OMe, H, Br, and Cl), using a synthetic procedure that reliably provides a 1:1:1 ratio, enabling the controlled production of CuSCN-based complexes with an underlying 2D structure. The 1:1:1 ratio was confirmed by IR spectroscopy and TGA while phase purity was verified by PXRD. In addition, we report for the first time the crystal structure of $[Cu(SCN)(3\text{-}OMePy)]_n$, in which the Cu-SCN network forms a 2D buckled sheet (similar to silicene or blue phosphorene). The electronic energy levels of the complexes are found to be systematically tunable depending on the electron-donating/electron-accepting ability of the substituent in 3-XPy, affecting both the optical absorption and emission properties. The use of aromatic co-ligands enabled CuSCN derivatives to be active in the visible region. With the increasing electron-accepting ability of the substituent, the energy levels shifted downward, and the optical band gap decreased in size. The electronic band structures were further elucidated by DFT calculations, which showed that (when compared to CuSCN) the Cu-S character of the valence bands was retained whereas the conduction bands distinctly changed to the Py co-ligand states. We have demonstrated that modifications caused by the co-ligands can

systematically tailor the electronic properties of CuSCN, and we are currently working on developing thin-film and device fabrication techniques of these 2D CuSCN-based complexes. The novel properties of visible absorption/emission and accessible conduction band states are expected to expand the application space of CuSCN-based materials further.

4. METHODS

4.1. Materials and experimental methods

All reagents were purchased from Sigma-Aldrich or TCI Chemicals and used without purification. Attenuated total reflectance-Fourier transform infrared spectroscopy (ATR-FTIR) measurements were collected using a PerkinElmer Frontier FT-IR spectrometer (with a Universal ATR accessory) in the range of 4000–400 cm^{-1} equipped with a pure diamond crystal. Thermogravimetric analyses (TGA) were measured using a Rigaku Thermo-Gravimetric Analyzer TG DTA8122. The measurements were performed with a heating rate of 10 °C min^{-1} to 500 °C under 200 μL min^{-1} of N_2 flow. Elemental analyses were measured using a LECO TruSpec Micro Elemental Series instrument to determine the percentages of C, H, and N. Powder X-ray diffraction (PXRD) data were recorded using a Bruker D8 ADVANCE X-ray diffractometer with a Cu Kα X-ray source (λ = 1.54056 Å) operated at 40 kV and 40 mA. Single-crystal X-ray crystallographic data of $[Cu(SCN)(3\text{-}OMePy)]_n$ was collected at 150 K on a Bruker D8 VENTURE diffractometer (Mo Kα radiation, λ = 0.71073 Å). The APEX4 program was used to determine the unit cell parameters and for data collection. The structure was solved by intrinsic phasing with SHELXT and refined by the full-matrix least-squares method on F^2 using SHELXL as implemented in OLEX^2.[38] The ultraviolet-visible (UV-Vis) absorption spectra of powder samples were recorded by a PerkinElmer Lambda 1050 UV/VIS/NIR Spectrophotometer in the reflection mode. Photoluminescence spectroscopy (PL) and time-resolved PL were measured by an Edinburgh Instruments FLS980 spectrometer. The photoelectron yield spectra (PYS) for the determination of the VBM positions were recorded

using a RIKEN AC-2 photoelectron spectrometer. A deuterium lamp giving UV light with an energy range of 4.2-6.4 eV was employed as an excitation source. The data were recorded at a step of 0.1 eV, and the UV source intensity was adjusted between 10-40 nW.

4.2. Synthesis of $[Cu(SCN)(3\text{-}XPy)]_n$

$[Cu(SCN)(3\text{-}ClPy)]_n$ **1**

A white suspension CuSCN (1.5 mmol, 182.45 mg) was prepared in 3 ml acetonitrile. 3-Chloropyridine (3-ClPy) (3.0 mmol, 282 μL) was added dropwise into the solution. The mixture was sealed in a vial and stirred for 24 h at 70 °C. The suspended solid was collected by filtration, washed with diethyl ether (2 ml, 2 times), and then air-dried producing a yellow powder (298.92 mg, 1.27 mmol, 84.7%). ATR-IR (cm^{-1}): 2119, 1412, 1111, 797, 740, 691. Elemental analysis calculated (%): C, 30.64; H, 1.71; N, 11.91. Found C, 30.3; H, 1.93; N, 11.8.

$[Cu(SCN)(3\text{-}BrPy)]_n$ **2**

A similar procedure for the synthesis of **1** was followed using 3-bromopyridine (3-BrPy) (3.0 mmol, 289 μL) producing a yellow powder (371.68 mg, 1.33 mmol, 88.6%). ATR-IR (cm^{-1}): 2117, 1463, 1415, 793, 689. Elemental analysis calculated (%): C, 25.77; H, 1.44; N, 10.02. Found C, 25.8; H, 1.41; N, 10.1.

$[Cu(SCN)(Py)]_n$ **3**

A similar procedure for the synthesis of **1** was followed using pyridine (Py) (3.0 mmol, 242 μL) producing a pale greenish yellow powder (258.53 mg, 1.28 mmol, 85.9%). ATR-IR (cm^{-1}): 2117, 1595, 1480, 1443, 748, 693. Elemental analysis calculated (%): C, 35.90; H, 2.51; N, 13.96. Found C, 35.6; H, 2.36; N, 14.2.

$[Cu(SCN)(3\text{-}OMePy)]_n$ **4**

A similar procedure for the synthesis of **1** was followed using 3-methoxypyridine (3-OMePy) (3.0 mmol, 303 μL) producing a pale yellow powder (313.49 mg, 1.35 mmol, 90.6%). ATR-IR (cm^{-1}): 2117, 1577, 1483, 1429, 794, 694. Elemental analysis calculated (%): C, 36.44; H, 3.06; N, 12.14. Found C, 36.2; H, 3.06; N, 12.2. The mother liquid was allowed to undergo slow evaporation over the course of a week to facilitate the formation of single crystals.

Reference $[Cu(SCN)]_n$ **5**

A powder sample of CuSCN (2.0 mmol, 243.26 mg) was prepared by a similar procedure for the synthesis of **1** without the addition of co-ligands producing a white powder (220.39 mg, 1.81 mmol, 90.6%). ATR-IR (cm^{-1}) 2170, 870, 746. Elemental analysis calculated (%): C, 9.87; N, 11.52. Found C, 10.2; N, 11.5.

4.3. Computational methods

First-principles calculations using the framework of density functional theory (DFT) were carried out with Vienna Ab initio Simulation Package (VASP).[39] The exchange-correlation interactions were modeled using the Perdew-Burke-Ernzerhof (PBE) functional within the generalized gradient approximation (GGA) and the Heyd-Scuseria-Ernzerhof (HSE06) hybrid functional.[40–42] The projector augmented wave (PAW) method,[43] employing a plane-wave basis set, was utilized. The kinetic energy cutoff was set to 520 eV, and the convergence criteria for energy and force on each ion were established at 1×10^{-5} eV and 0.01 eV $Å^{-1}$, respectively. The van der Waals (vdW) interactions were accounted for using Grimme's DFT-D3 correction.[44] The *k*-points in the reciprocal space were sampled using the Γ-centered Monkhorst-Pack scheme with a spacing of 0.03 (2π) $Å^{-1}$ for the PBE functional and 0.06 (2π) $Å^{-1}$ for the HSE06 hybrid functional.[45] The isosurfaces of charge densities (ρ) corresponding to the electronic band states at the valence band maximum and the conduction band minimum were visualized using VESTA software at the isosurface value of $\langle|\rho|\rangle + 1 \times \sigma(|\rho|)$, where $\langle|\rho|\rangle$ is the average and $\sigma(|\rho|)$ is the standard deviation of $|\rho|$.[46]

Author contributions

Jetnipat Songkerdthong: methodology, investigation, formal analysis, validation, visualization, writing – original draft. *Thanasee Thanasarnsurapong*: methodology, investigation, formal analysis (computational section). *Adisak Boonchun*: methodology, validation, resources, supervision, writing – review & editing (computational section). *David J. Harding*: validation, supervision, writing – review & editing. *Pichaya Pattanasattayavong*: conceptualization, funding acquisition, resources, supervision, validation, visualization, writing – review & editing, project administration.

Conflicts of interest

There are no conflicts to declare.

Acknowledgements

This research is funded by National Research Council of Thailand (NRCT), grant no. N42A650255 and N42A650196. This material is based upon work supported by the Air Force Office of Scientific Research under award number FA2386-22-1-4082. J.S. and P.P. acknowledge Vidyasirimedhi Institute of Science and Technology (VISTEC) for PhD scholarship and research funding and VISTEC's Frontier Research Center (FRC) for scientific instruments. We wish to thank Thailand's National Science and Technology Development Agency (NSTDA) Supercomputer Center (ThaiSC) for providing computing resources for this work. Dr. Chokchai Kaiyasuan and Pattarapapa Janthakit from VISTEC are acknowledged for their help with PL experiments.

References

(1) Pattanasattayavong, P.; Yaacobi-Gross, N.; Zhao, K.; Ndjawa, G. O. N.; Li, J.; Yan, F.; O'Regan, B. C.; Amassian, A.; Anthopoulos, T. D. Hole-Transporting Transistors and Circuits Based on the Transparent Inorganic Semiconductor Copper(I) Thiocyanate (CuSCN) Processed from Solution at Room Temperature. *Adv. Mater.* **2013**, *25* (10), 1504–1509. https://doi.org/https://doi.org/10.1002/adma.201202758.

(2) Petti, L.; Pattanasattayavong, P.; Lin, Y. H.; Münzenrieder, N.; Cantarella, G.; Yaacobi-Gross, N.; Yan, F.; Tröster, G.; Anthopoulos, T. D. Solution-Processed p-Type Copper(I) Thiocyanate (CuSCN) for Low-Voltage Flexible Thin-Film Transistors and Integrated Inverter Circuits. *Appl. Phys. Lett.* **2017**, *110* (11), 113504. https://doi.org/10.1063/1.4978531.

(3) Jaffe, J. E.; Kaspar, T. C.; Droubay, T. C.; Varga, T.; Bowden, M. E.; Exarhos, G. J. Electronic and Defect Structures of CuSCN. *J. Phys. Chem. C* **2010**, *114* (19), 9111–9117. https://doi.org/10.1021/jp101586q.

(4) Ji, Y.; Lee, S.; Lee, H. J.; Choi, K. S.; Jeon, C.; Lee, K. H.; Hong, K. Solution Processed Vertical P-Channel Thin Film Transistors Using Copper(i) Thiocyanate. *J. Mater. Chem. C* **2020**, *8* (16), 5587–5593. https://doi.org/10.1039/d0tc00815j.

(5) Perumal, A.; Faber, H.; Yaacobi-Gross, N.; Pattanasattayavong, P.; Burgess, C.; Jha, S.; McLachlan, M. A.; Stavrinou, P. N.; Anthopoulos, T. D.; Bradley, D. D. C. High-Efficiency, Solution-Processed, Multilayer Phosphorescent Organic Light-Emitting Diodes with a Copper Thiocyanate Hole-Injection/Hole-Transport Layer. *Adv. Mater.* **2015**, *27* (1), 93–100. https://doi.org/https://doi.org/10.1002/adma.201403914.

(6) Luo, W.; Zeng, C.; Du, X.; Leng, C.; Yao, W.; Shi, H.; Wei, X.; Du, C.; Lu, S. Copper Thiocyanate/Copper Iodide Based Hole Transport Composites with Balanced Properties for Efficient Polymer Light-Emitting Diodes. *J. Mater. Chem. C* **2018**, *6* (18), 4895–4902. https://doi.org/10.1039/c7tc04842d.

(7) Chavhan, S. D.; Ou, T. H.; Jiang, M. R.; Wang, C. W.; Jou, J. H. Enabling High-Efficiency Organic Light-Emitting Diode with Trifunctional Solution-Processable Copper(I) Thiocyanate. *J. Phys. Chem. C* **2018**, *122* (33), 18836–18840. https://doi.org/10.1021/acs.jpcc.8b05029.

(8) Georgiadou, D. G.; Wijeyasinghe, N.; Solomeshch, O.; Tessler, N.; Anthopoulos, T. D. Radiofrequency Schottky Diodes Based on P-Doped Copper(I) Thiocyanate (CuSCN). *ACS Appl. Mater. Interfaces* **2022**, *14* (26), 29993–29999. https://doi.org/10.1021/acsami.1c22856.

(9) Yaacobi-Gross, N.; Treat, N. D.; Pattanasattayavong, P.; Faber, H.; Perumal, A. K.; Stingelin, N.; Bradley, D. D. C.; Stavrinou, P. N.; Heeney, M.; Anthopoulos, T. D. High-Efficiency Organic Photovoltaic Cells Based on the Solution-Processable Hole Transporting Interlayer Copper Thiocyanate (CuSCN) as a Replacement for PEDOT:PSS. *Adv. Energy Mater.* **2015**, *5* (3), 1401529. https://doi.org/10.1002/aenm.201401529.

(10) Chaudhary, N.; Chaudhary, R.; Kesari, J. P.; Patra, A.; Chand, S. Copper Thiocyanate (CuSCN): An Efficient Solution-Processable Hole Transporting Layer in Organic Solar Cells. *J. Mater. Chem. C* **2015**, *3* (45), 11886–11892. https://doi.org/10.1039/c5tc03124a.

(11) Treat, N. D.; Yaacobi-Gross, N.; Faber, H.; Perumal, A. K.; Bradley, D. D. C.; Stingelin, N.; Anthopoulos, T. D. Copper Thiocyanate: An Attractive Hole Transport/Extraction Layer for Use in Organic Photovoltaic Cells. *Appl. Phys. Lett.* **2015**, *107* (1), 013301. https://doi.org/10.1063/1.4926408.

(12) Wijeyasinghe, N.; Regoutz, A.; Eisner, F.; Du, T.; Tsetseris, L.; Lin, Y. H.; Faber, H.; Pattanasattayavong, P.; Li, J.; Yan, F.; McLachlan, M. A.; Payne, D. J.; Heeney, M.; Anthopoulos, T. D. Copper(I) Thiocyanate (CuSCN) Hole-Transport Layers Processed from Aqueous Precursor Solutions and Their Application in Thin-Film Transistors and

Highly Efficient Organic and Organometal Halide Perovskite Solar Cells. *Adv. Funct. Mater.* **2017**, *27* (35), 1701818. https://doi.org/10.1002/adfm.201701818.

(13) Arora, N.; Dar, M. I.; Hinderhofer, A.; Pellet, N.; Schreiber, F.; Zakeeruddin, S. M.; Grätzel, M. Perovskite Solar Cells with CuSCN Hole Extraction Layers Yield Stabilized Efficiencies Greater than 20%. *Science* **2017**, *358* (6364), 768–771. https://doi.org/10.1126/science.aam5655.

(14) Chen, J.; Park, N. G. Inorganic Hole Transporting Materials for Stable and High Efficiency Perovskite Solar Cells. *J. Phys. Chem. C* **2018**, *122* (25), 14039–14063. https://doi.org/10.1021/acs.jpcc.8b01177.

(15) Sun, J.; Zhang, N.; Wu, J.; Yang, W.; He, H.; Huang, M.; Zeng, Y.; Yang, X.; Ying, Z.; Qin, G.; Shou, C.; Sheng, J.; Ye, J. Additive Engineering of the CuSCN Hole Transport Layer for High-Performance Perovskite Semitransparent Solar Cells. *ACS Appl. Mater. Interfaces* **2022**, *14* (46), 52223–52232. https://doi.org/10.1021/acsami.2c18120.

(16) Worakajit, P.; Sudyoadsuk, T.; Promarak, V.; Saeki, A.; Pattanasattayavong, P. Antisolvent Treatment of Copper(i) Thiocyanate (CuSCN) Hole Transport Layer for Efficiency Improvements in Organic Solar Cells and Light-Emitting Diodes . *J. Mater. Chem. C* **2021**, *9* (32), 10435–10442. https://doi.org/10.1039/d1tc02897a.

(17) Worakajit, P.; Hamada, F.; Sahu, D.; Kidkhunthod, P.; Sudyoadsuk, T.; Promarak, V.; Harding, D. J.; Packwood, D. M.; Saeki, A.; Pattanasattayavong, P. Elucidating the Coordination of Diethyl Sulfide Molecules in Copper(I) Thiocyanate (CuSCN) Thin Films and Improving Hole Transport by Antisolvent Treatment. *Adv. Funct. Mater.* **2020**, *30* (36), 2002355. https://doi.org/10.1002/adfm.202002355.

(18) Worakajit, P.; Kidkhunthod, P.; Thanasarnsurapong, T.; Waiprasoet, S.; Nakajima, H.; Sudyoadsuk, T.; Promarak, V.; Boonchun, A.; Pattanasattayavong, P. Origin of Hole-Trapping States in Solution-Processed Copper(I) Thiocyanate and Defect-Healing by

I2 Doping. *Adv. Funct. Mater.* **2023**, *33* (25), 2209504. https://doi.org/10.1002/adfm.202209504.

(19) Pearson, R. G. Hard and Soft Acids and Bases. *J. Am. Chem. Soc.* **1963**, *85* (22), 3533–3539. https://doi.org/10.1021/ja00905a001.

(20) Pattanasattayavong, P.; Packwood, D. M.; Harding, D. J. Structural Versatility and Electronic Structures of Copper(i) Thiocyanate (CuSCN)-Ligand Complexes. *J. Mater. Chem. C* **2019**, *7* (41), 12907–12917. https://doi.org/10.1039/c9tc03198g.

(21) Miller, K. M.; McCullough, S. M.; Lepekhina, E. A.; Thibau, I. J.; Pike, R. D.; Li, X.; Killarney, J. P.; Patterson, H. H. Copper(I) Thiocyanate-Amine Networks: Synthesis, Structure, and Luminescence Behavior. *Inorg. Chem.* **2011**, *50* (15), 7239–7249. https://doi.org/10.1021/ic200821f.

(22) Ayala, G.; Tronic, T. A.; Pike, R. D. Copper(I) Thiocyanate Networks with Aromatic Diimine Ligands. *Polyhedron* **2016**, *115*, 257–263. https://doi.org/10.1016/j.poly.2016.05.030.

(23) Nicholas, A. D.; Otten, B. M.; Ayala, G.; Hutchinson, J.; Wojtas, L.; Omary, M. A.; Pike, R. D.; Patterson, H. H. Light-Induced Photochemical Changes in Copper(I) Thiocyanate Complexes Decorated with Halopyridines: Optical Memory Manifestation. *J. Phys. Chem. C* **2017**, *121* (45), 25430–25439. https://doi.org/10.1021/acs.jpcc.7b06871.

(24) Tunsrichon, S.; Chainok, K.; Promarak, V.; Nalaoh, P.; Youngme, S.; Boonmak, J. Simultaneous Occurrence of Vapochromism and Vapoluminescence in Formaldehyde-Responsive Amino-Functionalized Copper(I) Polymorphic Coordination Polymers. *Inorg. Chem.* **2022**, *61* (30), 11734–11745. https://doi.org/10.1021/acs.inorgchem.2c01421.

(25) Yang, I. S.; Lee, S.; Choi, J.; Jung, M. T.; Kim, J.; Lee, W. I. Enhancement of Open

Circuit Voltage for CuSCN-Based Perovskite Solar Cells by Controlling the Perovskite/CuSCN Interface with Functional Molecules. *J. Mater. Chem. A* **2019**, *7* (11), 6028–6037. https://doi.org/10.1039/c8ta12217b.

(26) Xu, P.; Liu, J.; Huang, J.; Yu, F.; Zhang, R.; Li, C. H.; Zheng, Y. X.; Zuo, J. L.; Pan Xu, Jian Liu,* Jiahao Huang, Fan Yu, Rui Zhang, Cheng-Hui Li, You-Xuan Zheng, and J.-L. Z. Coordination Strategy Driving the Formation of Compact CuSCN Hole-Transporting Layers for Efficient Perovskite Solar Cells. *Sol. RRL* **2021**, *5* (5), 2000777. https://doi.org/10.1002/solr.202000777.

(27) Krautscheid, H.; Emig, N.; Klaassen, N.; Seringer, P. Thiocyanato Complexes of the Coinage Metals: Synthesis and Crystal Structures of the Polymeric Pyridine Complexes [AgxCuy(SCN)X+y(Py)Z]. *J. Chem. Soc. - Dalt. Trans.* **1998**, *1* (18), 3071–3077. https://doi.org/10.1039/a803468k.

(28) Wang, B.; Nam, S.; Limbu, S.; Kim, J. S.; Riede, M.; Bradley, D. D. C. Properties and Applications of Copper(I) Thiocyanate Hole-Transport Interlayers Processed from Different Solvents. *Adv. Electron. Mater.* **2022**, *8* (7), 2101253. https://doi.org/10.1002/aelm.202101253.

(29) Ayala, G.; Pike, R. D. Copper(I) Thiocyanate Networks with Aliphatic Sulfide Ligands. *Polyhedron* **2016**, *115*, 242–246. https://doi.org/10.1016/j.poly.2016.05.029.

(30) Yang, Z.; Wu, B.; Zhai, C.; Niu, S.; Sun, B.; Dang, L.; Gu, C.; Qi, X.; Tian, Y.; Li, J.; Ma, S.; Yao, M. Pressure-Dependent Structural and Band Gap Tuning of Semiconductor Copper(I) Thiocyanate (CuSCN). *Inorg. Chem.* **2022**, *61* (48), 19274–19281. https://doi.org/10.1021/acs.inorgchem.2c03024.

(31) Bowmaker, G. A.; Hanna, J. V. IR Spectroscopy of Two Polymorphs of Copper(I) Thiocyanate and of Complexes of Copper(I) Thiocyanate with Thiourea and Ethylenethiourea. *Z. Naturforsch.* **2009**, *64* (11–12), 1478–1486. https://doi.org/10.1515/znb-2009-11-1231.

(32) Miró, P.; Audiffred, M.; Heine, T. An Atlas of Two-Dimensional Materials. *Chem. Soc. Rev.* **2014**, *43* (18), 6537–6554. https://doi.org/10.1039/c4cs00102h.

(33) Xu, Y.; Shi, Z.; Shi, X.; Zhang, K.; Zhang, H. Recent Progress in Black Phosphorus and Black-Phosphorus-Analogue Materials: Properties, Synthesis and Applications. *Nanoscale* **2019**, *11* (31), 14491–14527. https://doi.org/10.1039/c9nr04348a.

(34) Galicia Hernandez, J. M.; Fernandez-Escamilla, H. N.; Guerrero Sanchez, J.; Takeuchi, N. Electronic and Optical Properties of the Buckled and Puckered Phases of Phosphorene and Arsenene. *Sci. Rep.* **2022**, *12* (1), 1–14. https://doi.org/10.1038/s41598-022-24425-w.

(35) Yang, L.; Powell, D. R.; Houser, R. P. Structural Variation in Copper(i) Complexes with Pyridylmethylamide Ligands: Structural Analysis with a New Four-Coordinate Geometry Index, T4. *J. Chem. Soc. Dalt. Trans.* **2007**, No. 9, 955–964. https://doi.org/10.1039/b617136b.

(36) Janiak, C. A Critical Account on N-n Stacking in Metal Complexes with Aromatic Nitrogen-Containing Ligands. *J. Chem. Soc. Dalt. Trans.* **2000**, No. 21, 3885–3896. https://doi.org/10.1039/b003010o.

(37) Borlido, P.; Schmidt, J.; Huran, A. W.; Tran, F.; Marques, M. A. L.; Botti, S. Exchange-Correlation Functionals for Band Gaps of Solids: Benchmark, Reparametrization and Machine Learning. *npj Comput. Mater.* **2020**, *6* (1), 96. https://doi.org/10.1038/s41524-020-00360-0.

(38) Dolomanov, O. V.; Bourhis, L. J.; Gildea, R. J.; Howard, J. A. K.; Puschmann, H. OLEX2: A Complete Structure Solution, Refinement and Analysis Program. *J. Appl. Cryst.* **2009**, *42* (2), 339–341. https://doi.org/10.1107/S0021889808042726.

(39) Kresse, G.; Furthmüller, J. Efficient Iterative Schemes for Ab Initio Total-Energy Calculations Using a Plane-Wave Basis Set. *Phys. Rev. B - Condens. Matter Mater.*

Phys. **1996**, *54* (16), 11169–11186. https://doi.org/10.1103/PhysRevB.54.11169.

(40) Perdew, J. P.; Burke, K.; Ernzerhof, M. Generalized Gradient Approximation Made Simple. *Phys. Rev. Lett.* **1996**, *77* (18), 3865–3868. https://doi.org/10.1103/PhysRevLett.77.3865.

(41) Heyd, J.; Scuseria, G. E.; Ernzerhof, M. Hybrid Functionals Based on a Screened Coulomb Potential. *J. Chem. Phys.* **2003**, *118* (18), 8207–8215. https://doi.org/10.1063/1.1564060.

(42) Heyd, J.; Scuseria, G. E.; Ernzerhof, M. Erratum: Hybrid Functionals Based on a Screened Coulomb Potential (Journal of Chemical Physics (2003) 118 (8207)). *J. Chem. Phys.* **2006**, *124* (21), 219906. https://doi.org/10.1063/1.2204597.

(43) Blöchl, P. E. Projector Augmented-Wave Method. *Phys. Rev. B* **1994**, *50* (24), 17953–17979. https://doi.org/10.1103/PhysRevB.50.17953.

(44) Grimme, S.; Antony, J.; Ehrlich, S.; Krieg, H. A Consistent and Accurate Ab Initio Parametrization of Density Functional Dispersion Correction (DFT-D) for the 94 Elements H-Pu. *J. Chem. Phys.* **2010**, *132* (15), 154104. https://doi.org/10.1063/1.3382344.

(45) Pack, J. D.; Monkhorst, H. J. Special Points for Brillouin-Zone Integrations. *Phys. Rev. B* **1976**, *13* (4), 5188–5192. https://doi.org/10.1103/PhysRevB.16.1748.

(46) Momma, K.; Izumi, F. VESTA 3 for Three-Dimensional Visualization of Crystal, Volumetric and Morphology Data. *J. Appl. Cryst.* **2011**, *44*, 1272–1276. https://doi.org/10.1107/S0021889811038970.